Nanoscale

PAPER

View Article Online
View Journal | View Issue

Cite this: *Nanoscale*, 2025, **17**, 27350

Multi-stimuli responsive nanomaterials assembled from spiropyran-containing peptoids

Progyateg Chakma, [a,b] Bradley S. Harris, [a] Chenyang Shi, [a] Botao Hao, [a] Kyle Whitaker,[b] Marcel D. Baer [a] and Chun-Long Chen *[a,c]

Received 17th August 2025,
Accepted 7th November 2025

DOI: 10.1039/d5nr03491d

rsc.li/nanoscale

Stimuli-responsive tunable supramolecular assemblies are highly desirable for controlling functionalities *via* morphological changes and alternations in crystallinity. Here, we report that amphiphilic peptoids with a multifunctional spiropyran (SP) group assemble into responsive 2D nanosheets and 1D nanotubes through light and heat-mediated isomerization. Computational analysis by periodic density functional theory (DFT) calculations on dimers of SP and its isomer, merocyanine (MC), reveals significantly more favorable packing energetics for MC compared to SP, further supporting the high crystallinity of assemblies composed of peptoids with MC. Furthermore, we demonstrate how stimulus-responsive control over peptoid assembly crystallinity can be utilized in tuning catalytic activity in mimicking carbonic anhydrase (CA) enzymes.

Introduction

Molecular self-assembly into supramolecular structures is essential for creating functionality in biological systems.[1–4] Inspired by nature, significant efforts in supramolecular chemistry and materials science have focused on constructing synthetic supramolecular assemblies with sophisticated and complex functions.[1–3,5,6] In particular, there is considerable interest in stimuli-responsive assemblies of organic molecules, which can be modulated to achieve specific morphologies and functionalities.[1,7–9] Often, the macroscopic properties of these supramolecular assemblies can be reversibly manipulated through external stimuli such as light, pH value, heat, mechanical force, and salts.[1,3,10] In particular, light as a stimulus has significant advantages, as it can be applied to a specific location with responsive moieties activated at different wavelengths, with varying energy input, and in different directions.[11–13] Among the photoswitches, spiropyran (SP) is highly unique as it reversibly isomerizes into the "open-ring" merocyanine (MC) form, exhibiting significant changes in physicochemical properties.[14,15] For example, SP is a non-polar and non-planar molecule. In contrast, isomerization into MC induces a planar structure with extended pi–pi interaction and a change in dipole moments (from ~4–6 D to ~14–18 D) (Fig. 1). Interestingly, in addition to being a photoswitch, reversible SP to MC isomerization can be induced further by temperature, mechanical force, solvent polarity, pH, metal ions, and ionic concentration.[14,16] The light-triggered pH switch enables the transition between SP and MC, affording Sp-containing materials with great potential in applications such as CO_2 capture and sequestration.[13,17,18] Due to their multi-stimuli-responsive and multifunctional properties, SP moieties have been frequently explored and utilized to construct stimuli-responsive functional materials.[14,19–22] However, minimal effort has been made to connect SPs with sequence-defined synthetic polymers for the development of biomimetic materials with multi-stimuli responsiveness and protein-like high information content.

Peptoids, known as poly-*N*-substituted glycines, are a type of well-advanced, sequence-defined peptidomimetics.[1,2,23,24] Unlike peptides, where self-assembly is primarily driven by hydrogen bonding, peptoids rely on controlled hydrophobic interactions and side-chain chemistry for their self-assembly. This leads to enhanced stability while maintaining biocompatibility.[1,2,23,25] Recently, we and others have designed and synthesized a series of amphiphilic peptoids that self-assemble into highly crystalline, hierarchical nanomaterials with various morphologies and functionalities, as well as excellent chemical and thermal stability.[1,2,25–27] In particular, peptide- and peptoid-based stimuli-responsive biomaterials have recently gained significant attention due to their excellent prospects in biomedical and biotechnology applications.[1,2,6,28] However, SP has never been used as a functional group for the development of responsive peptoid assembly materials.

[a]*Physical Sciences Division, Pacific Northwest National Laboratory, Richland, WA 99352, USA. E-mail: Chunlong.Chen@pnnl.gov*
[b]*Department of Chemistry and Biochemistry, Kennesaw State University, Kennesaw, GA 30144, USA*
[c]*Department of Chemical Engineering, University of Washington, Seattle, WA 98195, USA*

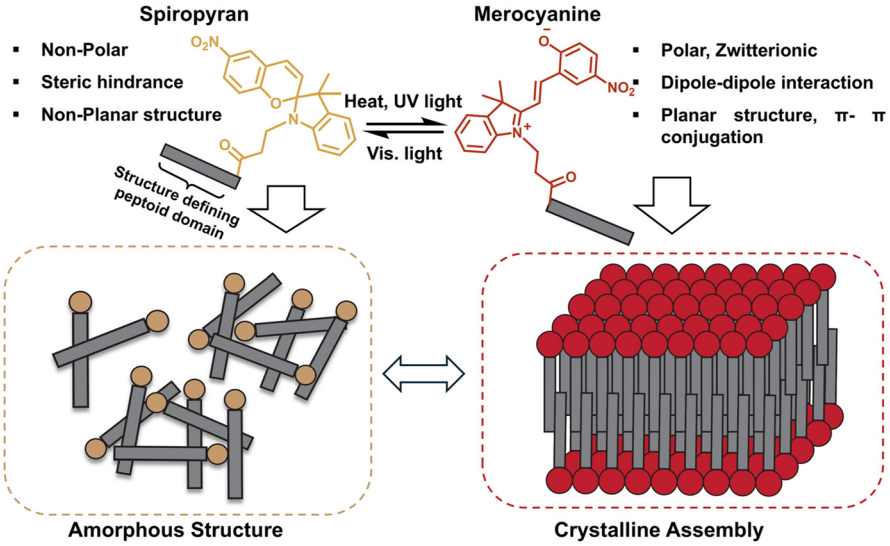

Fig. 1 Stimuli-responsive reversible transformation of spiropyran and merocyanine and their functionalization into peptoids, leading to tunable control of assembly into supramolecular structures.

Here, for the first time, we report the covalent attachment of SP at the N-terminus of self-assembling peptoids for the development of light- and heat-responsive peptoid nanomaterials with nanosheet or nanotube morphologies. We demonstrate that assembly morphology and crystallinity of these peptoid nanomaterials can be modulated through light- and heat-mediated SP and MC isomerization (Fig. 1). To better understand the molecular origin of these stimuli-responsive behaviors, we also performed quantum chemical calculations on representative SP and MC dimer structures. These computations reveal distinct energetic preferences for MC-based stacking, which help rationalize the experimentally observed differences in crystallinity and assembly kinetics. Finally, we explored how stimulus-responsive control of the crystallinity of assembled peptoid nanomaterials can be utilized to tune catalytic activity in mimicking carbonic anhydrase (CA) enzymes.

Results and discussion

Design and synthesis of peptoid sequences conjugated with a spiropyran group

To study the effect of reversible photochromism of SP, we designed and synthesized amphiphilic peptoids with either six Nbrpe = *N*-([2-(4-bromophenyl)ethyl]glycine) or Nbrpm = *N*-[(4-bromophenyl)methyl] glycine were introduced as side chains for the hydrophobic domains that are responsible for assembly into highly crystalline nanosheets or nanotubes *via* aromatic interactions.[2,27,29–33] Here, the π–π interaction of phenyl rings in six Nbrpe groups leads to the formation of a flat, sheet-like structure.[29,34–36] In contrast, the molecular packing of peptoids containing six Nbrpm groups leads to the formation of a tubular structure.[26,27,30,35,37–39] On the other hand, two [2-(4-imidazolyl)ethyl]glycine (Nhis) were introduced in the polar domain to help with solubility and processability. Here, in addition to facilitating solubility, Nhis side chain was used to mimic the active sites of carbonic anhydrase (CA) enzymes, thus creating responsive CA-mimics for enhanced CO_2 hydration and sequestration.[35] Finally, the SP moiety was functionalized at the N-terminus of self-assembly peptoids to study the effect of changes in polarity, solubility, steric, and supramolecular interactions through reversible SP to MC photochromism. We hypothesized that, while the self-assembly of amphiphilic peptoids into crystalline nanomaterials is dominated by enhanced hydrophobic interactions (*e.g.*, π–π stacking) among hydrophobic domains,[40–45] drastic changes in the physicochemical properties of the functional group at the N-terminus can significantly influence the properties of the peptoid assembly process. Peptoids with Nbrpe, Nbrpm, and Nhis side chains are shown in Fig. 2A. All peptoids were synthesized using the submonomer solid-phase synthesis method previously reported by our group.[26,27,32,46] Synthesized peptoids were purified using reverse-phase high-performance liquid chromatography (HPLC), and their purity was confirmed by ultra-performance liquid chromatography equipped with mass spectrometry (UPLC-MS) (Fig. S1 and 2). The detailed synthesis and characterization methodology for these peptoids can be found in the Methods and SI sections.

Reversible isomerism of spiropyran-functionalized peptoids

Before proceeding with the self-assembly of the peptoids, we initially studied the reversible photochromism of SP to MC using ultraviolet–visible (UV-Vis) spectroscopy with Pep1 to determine optimum conditions for this transformation. In the presence of ambient visible light and room temperature, Pep1 remains in SP form (Pep1SP), as no characteristic MC absorbance is observed in the 500–550 nm region. Typically, UV irradiation is utilized to initiate SP to MC transformation.[14]

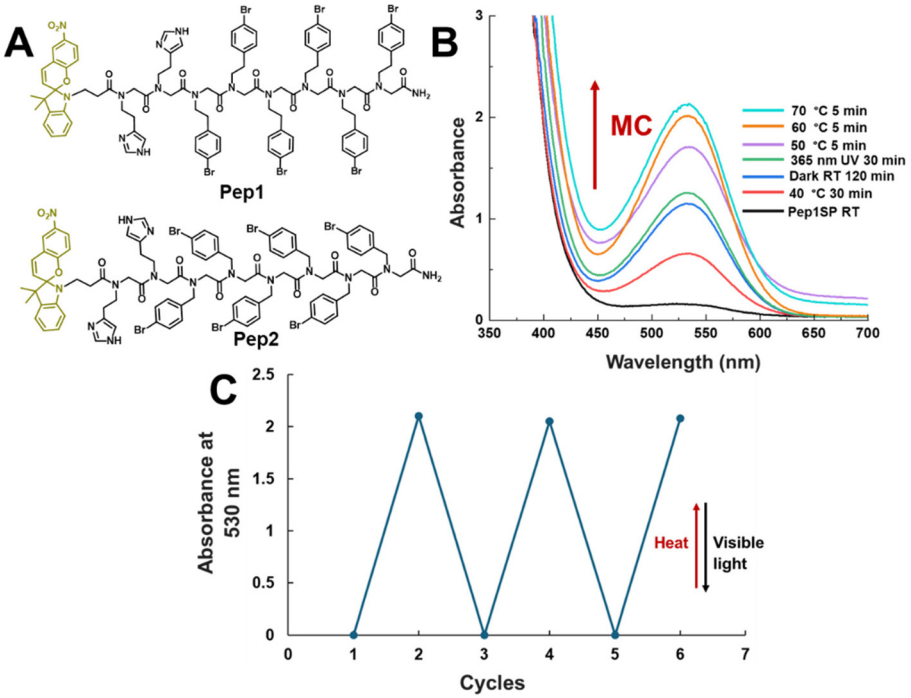

Fig. 2 (A) Peptoid sequences containing Nbrpe, Nbrpm, and Nhis side chains explored in this work, (B) multi-stimuli responsive changes in UV-Vis spectra of spiropyran-functionalized peptoid Pep1SP to Pep1MC in acetonitrile/water (0.1 mM in acetonitrile/water; v/v = 1 : 1), and (C) reversible photochromism of Pep1SP to Pep1MC (0.1 mM in acetonitrile/water) for consecutive cycles – firstly by heating at 70 °C for 15 min, then irradiated with ambient visible light for 5 min.

Interestingly, minimal success was observed when irradiating the Pep1SP solution (0.1 mM in acetonitrile/water; v/v = 1 : 1) with long-wavelength 365 nm UV light for 30 minutes or when leaving it in the absence of light, as shown in Fig. 2B. Recently, Wang *et al.* reported that the reverse photochromism of SP to MC can be effectively promoted by heating.[22] Inspired by their report, when the Pep1SP solution was heated from 40 °C to 70 °C, a significant increase in the characteristic MC absorbance at 530 nm was observed (Fig. 2B), indicating that the opening of the SP moiety and transformation to Pep1MC can be effectively mediated by relatively mild heating, without any UV irradiation. Interestingly, reverse transformation to Pep1SP was very rapid upon exposure to warm white light (1 minute) or ambient visible light (5 minutes). The heat-light-responsive SP to MC transformation can be repeated for at least three cycles without any noticeable degradation (Fig. S5).

Assembly of SP- and MC-peptoids

Based on the initial finding of heat-mediated, highly efficient transformation of SP to MC, we proceeded to study the self-assembly of Pep1 under different conditions. Typically, Pep1, containing six Nbrpe side groups, should lead to the formation of crystalline 2D nanosheets.[34–36,46] We were interested in studying how the incorporation of a bulky and non-polar SP moiety, followed by its transformation into a planar and polar MC isomer, affects the self-assembly properties of amphiphilic peptoids. For the assembly of Pep1SP, lyophilized peptoid powder was dissolved in a 1 : 1 (v/v) acetonitrile/water solution and left at 4 °C in the presence of ambient visible light to facilitate slow crystallization. On the other hand, for the assembly of Pep1MC, the Pep1MC solution in acetonitrile/water (v/v = 1 : 1) was heated at 60 °C for 20 minutes to facilitate the SP to MC transformation. A complete conversion of Pep1SP to Pep1MC was confirmed by UV-Vis spectroscopy. The resulting Pep1MC solution was then left at 4 °C in the dark to allow for slow evaporation, which triggered the self-assembly. Interestingly, a deep red, gel-like solution was obtained after about one week (Fig. S5). In contrast, the self-assembly of Pep1SP was much slower; a slightly yellowish, gel-like solution with slurry was obtained after at least two weeks of slow evaporation of the Pep1SP solution (Fig. S5). These results indicate that the MC form is much more favorable for the peptoid gelation (*i.e.*, crystallization) than the SP form. In contrast, in the SP form, self-assembly of Pep1 into crystalline nanosheets is very challenging. To assess the morphology of assembled Pep1MC and Pep1SP materials, atomic force microscopy (AFM), scanning electron microscopy (SEM), and transmission electron microscopy (TEM) were employed. Both AFM and SEM characterizations of the assembled Pep1MC materials (Fig. 3A and C) reveal the formation of 2D nanosheets with lateral dimensions exceeding 5.0 μm, straight edges, and a thickness of approximately 4.0 nm. The formation of such large 2D nanosheets was further confirmed by liquid-cell AFM and TEM characterizations (Fig. S7A and S7B). On the contrary,

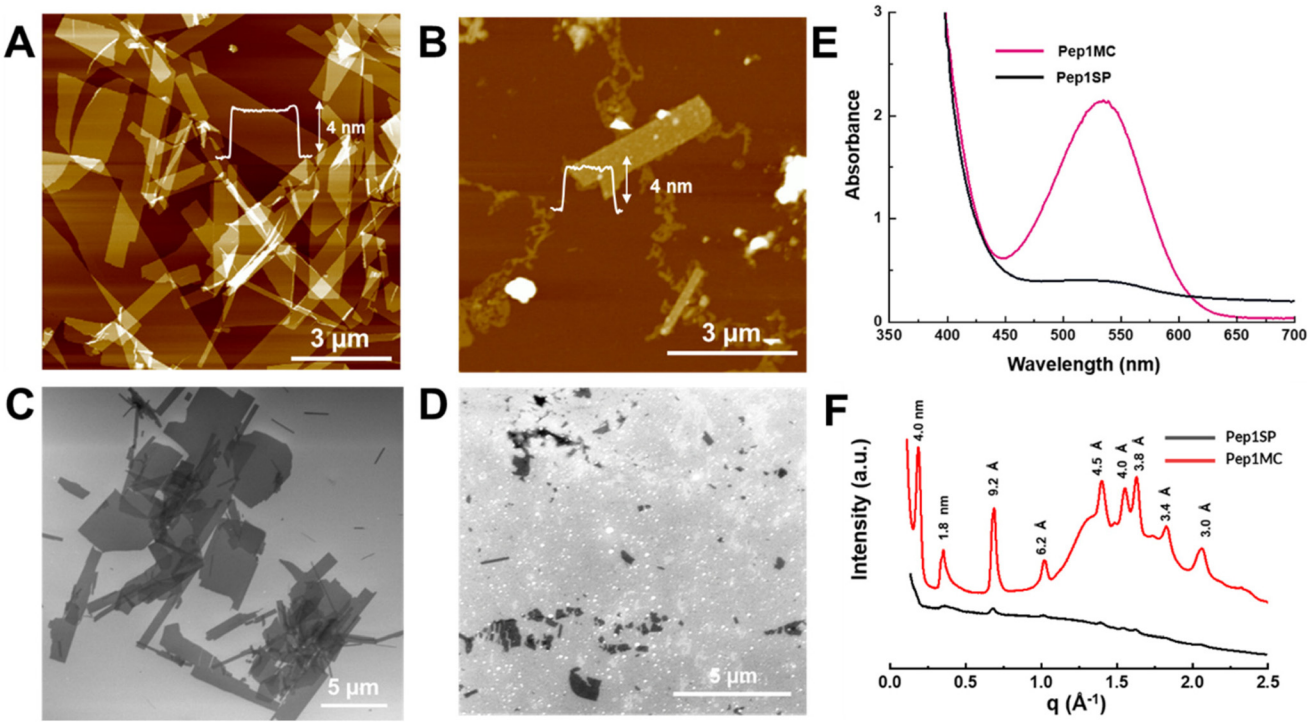

Fig. 3 Representative AFM images of assembled – (A) Pep1MC and (B) Pep1SP; in both cases, the height profile was used. Representative SEM images of assembled – (C) Pep1MC and (D) Pep1SP. (E) UV-Vis spectra of Pep1SP and Pep1MC (0.1 mM) in acetonitrile, and (F) Representative XRD data of assembled Pep1MC and Pep1SP. The values above each peak are the corresponding lattice spacing values.

AFM and SEM results show that assembled Pep1SP materials primarily consist of amorphous-like aggregates, with fewer nanosheets of approximately 4.0 nm thickness (Fig. 3B and D). UV-Vis spectroscopy analysis of the assembled Pep1SP and Pep1MC materials reveals that the majority of the self-assembling peptoid conjugate is in SP and MC forms, respectively (Fig. 3E), which is further confirmed by UPLC characterization (Fig. S10A and B). Interestingly, as seen in Fig. S8, the surface roughness of the nanosheets calculated from the AFM images of assembled Pep1MC and Pep1SP materials shows a significantly higher root mean square (RMS) roughness value (R_q) in Pep1SP sheets (R_q = 1.680 nm) than Pep1MC sheets (R_q = 0.108 nm). This indicates considerably greater height variation or a rougher surface in Pep1SP nanosheets compared to Pep1MC nanomaterials, resulting in high crystallinity and highly ordered functional groups. Finally, the crystallinity of the assembled Pep1MC and Pep1SP materials was evaluated by synchrotron-based X-ray diffraction (XRD) measurements. XRD data of Pep1MC materials confirm the high crystallinity of Pep1MC nanosheets, as evidenced by very sharp and distinct peaks (Fig. 3F), which are like those previously observed in the case of assembled nanosheets from other Nbrpe6-containing sequences.[29,36,46] Conversely, the XRD data of Pep1SP materials show a broad and diffuse pattern, suggesting low crystallinity (Fig. 3F). This experimental observation is further supported by periodic DFT calculations (See discussion below), which show that MC dimers are energetically more favorable than SP dimers for ordered packing due to their planar structure and favorable dipole alignment. To study how SP and MC moieties affect the assembly of these responsive peptoid conjugates, peptoid conjugates were self-assembled with a lower composition of MC. To achieve this, the Pep1SP solution was maintained at 4 °C in a dark environment, either without initial heating or after 2 hours of 365 nm long-wavelength UV irradiation. As no heat-promoted SP to MC transformation was involved in either case, the MC composition should be lower than that of the ideal heat-mediated transformation. AFM and SEM characterizations of these assembled samples show mainly amorphous-like structures with few nanosheet formations, albeit smaller in size than those of Pep1MC assembled nanosheets, indicating non-optimal assembly (Fig. S10). We postulate that this could be due to a comparatively lower composition of MC and the presence of the SP isomer in the Pep1 solution, as indicated by UPLC traces (Fig. S10C and D).

Encouraged by the effect of SP to MC transformation in nanosheet assembly, we further explored the influence of the reverse photochromism of SP on Pep2 containing six Nbrpm side chains (Fig. 2A). Typically, di-block-like peptoids containing six Nbrpm groups in the hydrophobic domain form 1D nanotubes. Pep2SP and Pep2MC were self-assembled in the same conditions as Pep1SP and Pep1MC. Similar to the assembly of sheet materials, a deep red, gel-like solution was obtained from Pep2MC after only one week of self-assembly. In contrast, a solution of aggregates and slurries was obtained from Pep2SP after at least three weeks of slow evaporation. *Ex*

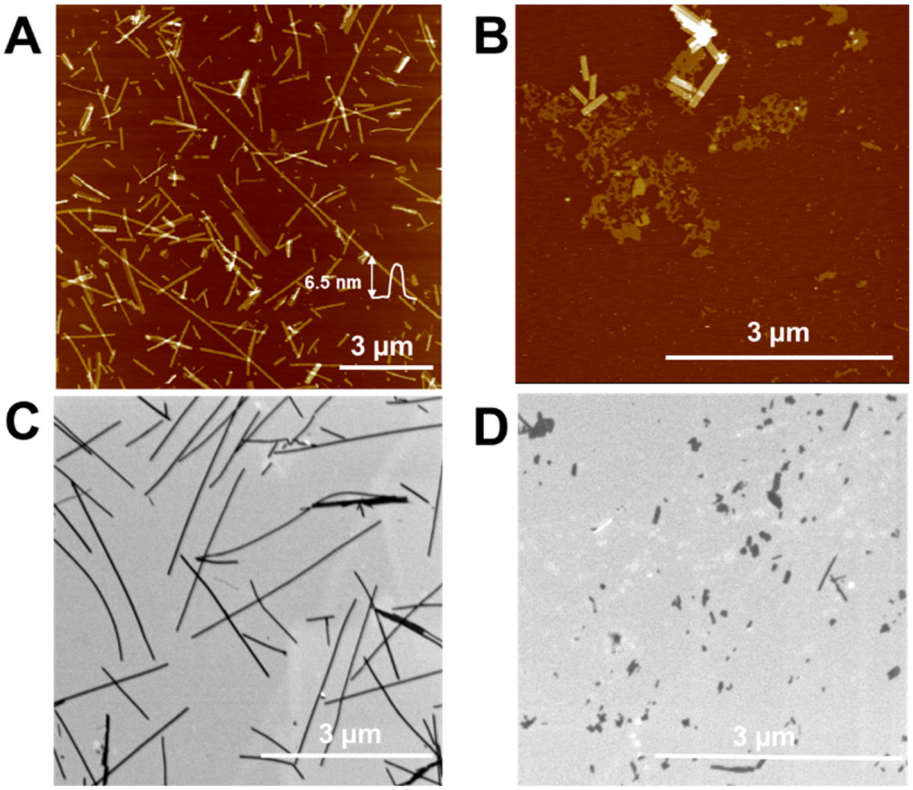

Fig. 4 Representative AFM images of assembled (A) Pep2MC and (B) Pep2SP. Representative SEM images of assembled (C) Pep2MC and (D) Pep2SP.

situ AFM characterization of Pep2MC gel-like materials reveals the formation of 1D nanotubes with a tube height of around 6.5 nm (Fig. 4A). Formation of uniform 1D nanotubes was further confirmed by liquid cell AFM (Fig. S6b) and SEM (Fig. 4C). Negatively stained transmission electron microscopy (TEM) images revealed that Pep2MC nanotubes have a wall thickness of 3.8 ± 0.6 nm and an average tube diameter of 30.9 ± 0.9 nm, similar to the previously reported tube thickness and average diameter of our peptoid nanotubes.[27,30,38] On the other hand, AFM and SEM results indicate that Pep2SP forms a very few smaller, non-uniform nanotubes, with mostly amorphous-like aggregates (Fig. 4B and D). Finally, XRD analysis of the assembled Pep2MC materials unveils high crystallinity of the nanotubes, characterized by very sharp and distinct peaks (Fig. S11), similar to the characteristic peaks observed in other nanotubes assembled from peptoids containing six Nbrpm groups.[27,30,38] On the contrary, the XRD data of Pep2SP assemblies reveal comparatively low crystallinity with broader peaks and a diffuse pattern (Fig. S11). To assess whether the SP to MC transformation induces similar effects on the assembly properties of amphiphilic peptoids lacking Nhis groups, Pep3 with six *N*-([2-(4-chlorophenyl)ethyl]glycine) (Nclpe) groups in the hydrophobic domain, and six *N*-(2-methoxyethyl)glycine (Nme) in the hydrophilic domain was synthesized (Fig. S3). Here, six Nme groups were used to assist with solubility. Like Pep1MC and Pep2MC, the assembly of the Pep3MC solution also resulted in the formation of crystalline nanosheets, as confirmed by AFM, SEM, and XRD results (Fig. S12). In contrast, amorphous materials were obtained from the Pep1SP (Fig. S12). These findings suggest that the transformation of bulky, sterically hindered, nonpolar SP moieties into polar and planar MC moieties, with MC–MC dipole–dipole and π-interactions, plays a key role in obtaining highly crystalline nanomaterials.

Light-responsive disassembly of MC-conjugated peptoid nanomaterials

After exploring the heat- and light-responsive assembly properties of SP-conjugated peptoids, we were intrigued to see how crystalline nanomaterials assembled from MC-conjugated peptoids would behave upon exposure to visible light. When the assembled Pep1MC gel solution was exposed to ambient visible light for different durations, a change from deep red to yellowish color was observed. AFM characterization of gel-like materials after being exposed to varying periods of ambient visible light exposure reveals the disassembly of peptoid nanosheets into amorphous-like materials (Fig. 5A–E). UV-Vis spectra of the assembled Pep1MC materials after 96 h of visible light exposure reveal the disappearance of the characteristic MC peak, suggesting the complete conversion of Pep1MC into Pep1SP (Fig. S13). We hypothesize that the disassembly of Pep1MC nanosheets may be due to the disruption of MC–MC interactions, resulting in significant changes in physicochemical properties, such as steric hindrance, polarity,

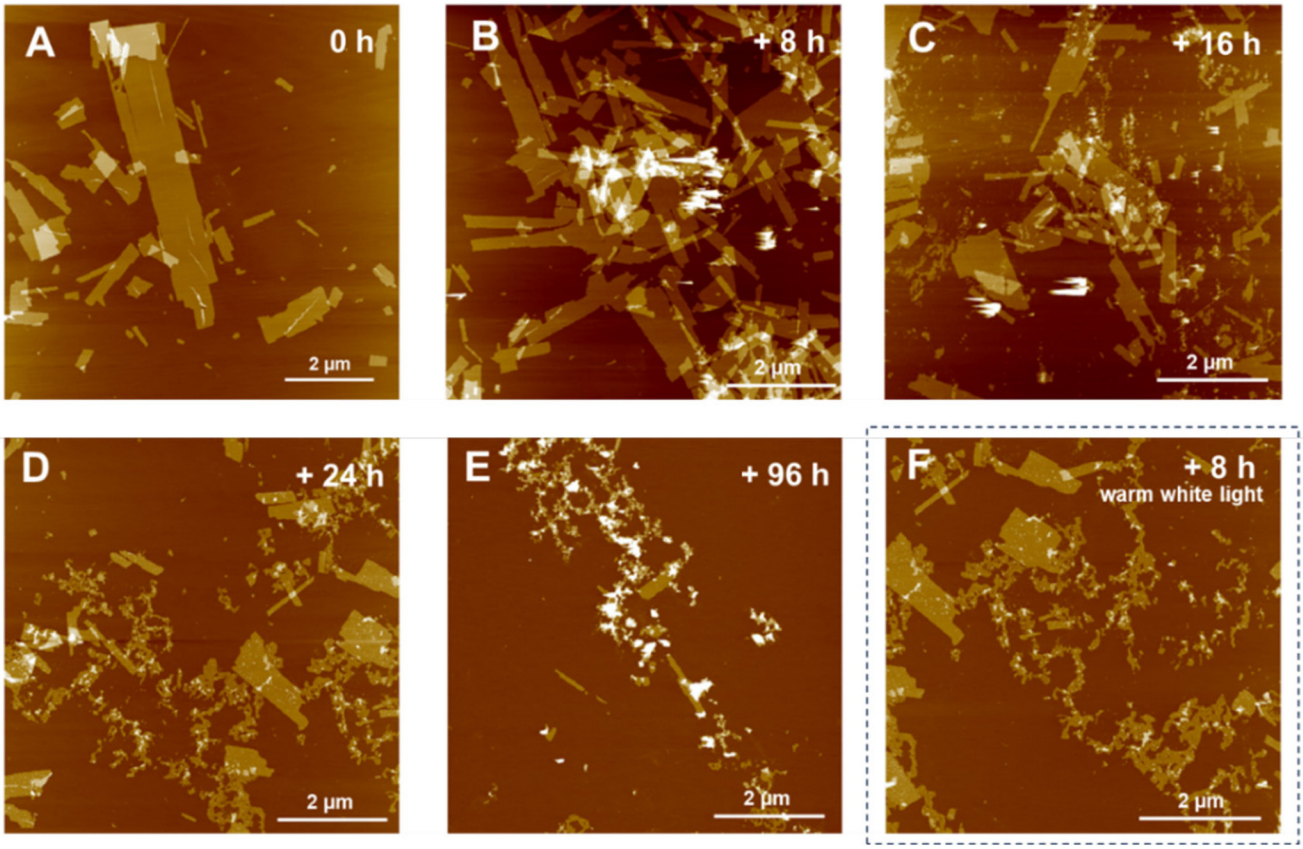

Fig. 5 Representative AFM images showing time-dependent change in crystallinity and assembly of Pep1MC, when exposed to ambient visible light (A–E), and warm white light (F).

and solubility, within the assembled nanomaterials. Interestingly, the disassembly process can be accelerated upon exposure to warm white light using a photoreactor (Fig. 5F). Nonetheless, the MC to SP conversion in the assembled materials was significantly slower than in the Pep1MC monomer solution. We hypothesize that this is likely attributed to the significant energy barrier associated with disrupting MC–MC interactions within the crystalline peptoid assemblies, required for their conversion to the close-ring spiropyran form. Additionally, the SP to MC transformation can occur spontaneously through "negative photochromism" in the absence of light, particularly in polar solvents such as water.[14,47] To evaluate that, when the aqueous solution of assembled Pep1SP materials was left in the absence of light for three weeks, a significantly high amount of nanosheets with nearly no amorphous-like materials was observed, as shown in the AFM characterization (Fig. S14). This result suggests that the conversion of Pep1SP to Pep1MC facilitates MC–MC interactions in a dark environment, thereby promoting the formation of nanosheets in aqueous solution. These findings were further confirmed by SEM results (Fig. S15). This light-responsive change in both assembly structures and crystallinity was further analyzed and confirmed by the XRD result (Fig. 6).

When the stability of Pep1MC nanosheets and Pep2MC nanotubes was studied in the absence of light at elevated temperatures or in organic solvents, it was found that both nanomaterials are stable and retain their nanostructures after heating or exposure to organic solvents (Fig. S16 and S17). These results suggest that MC-containing peptoid nanosheets and nanotubes, with MC functionality, retain their high stability in the absence of light, even at elevated temperatures or in the presence of excess organic solvents. These results are similar to those of our previously reported Peptoid assemblies, highlighting the unique advantages of these synthetic materials compared to biological systems.[2,27,32] Exposure to visible light irradiation is necessary for the transformation of PepMC to PepSP, leading to the disassembly of the PepMC crystalline nanomaterials. To further confirm that the disruption of MC–MC interactions and a significant change in the physicochemical property of self-assembling PepMC are responsible for the disassembly of peptoid crystalline nanomaterials, Pep1MC was co-assembled with Pep4, an amphiphilic peptoid similar to Pep1SP but without MC conjugation. Co-assembly of Pep4 with Pep1MC in an 80 : 20 ratio, *i.e.*, 80% Pep4 and 20% Pep1MC, resulted in the formation of crystalline nanosheets, as seen from AFM and SEM images (Fig. S18A and B) and SEM images (Fig. S18C and D). When these nanosheets were exposed to ambient visible light for 48 hours, no significant change in the assembly morphology was observed. We hypothesized that in the co-crystallization of Pep4 : Pep1MC

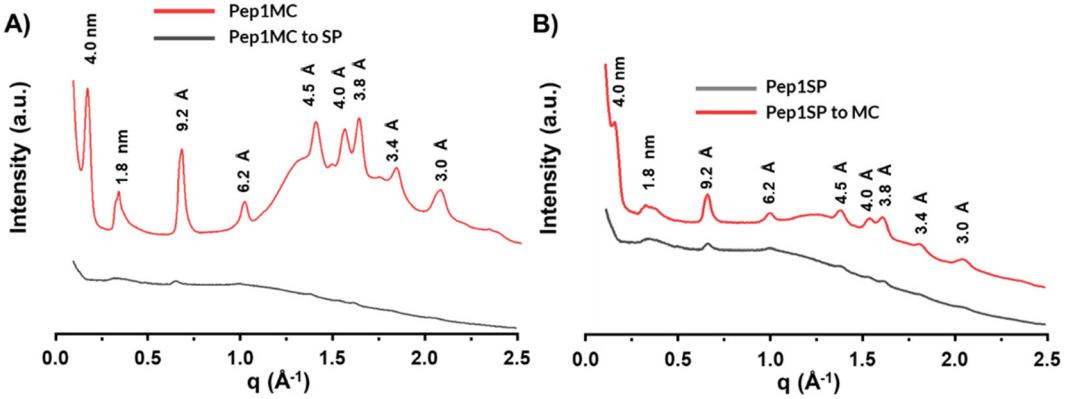

Fig. 6 XRD data of (A) Assembled Pep1MC nanosheets exposed to ambient visible light for 96 h, (B) assembled Pep1SP nanomaterials left in the dark for three weeks. Here, the values above each peak are the corresponding lattice spacing values.

(80 : 20), this process is primarily driven by hydrophobic interactions (*e.g.*, π–π interactions) among hydrophobic Nbrpe side chains.[40–45] Because this system contains only 20% Pep1MC, the low density of the MC group within the peptoid sheets makes MC–MC interactions unlikely.[48] As a result, upon exposure to visible light, no substantial change in physicochemical properties can be observed, leading to the retention of assembled crystalline nanostructures.

Computational analysis of SP and MC dimer packing energetics

To investigate the molecular basis for the enhanced crystallinity observed in MC-functionalized peptoids, we conducted density functional theory (DFT) calculations on representative dimer structures of both the SP and MC forms. These dimers were selected to mimic backbone-backbone packing motifs relevant to the experimentally observed assembled nanostructures.

For each isomer, the lowest-energy dimer conformations were used to construct periodic one-dimensional stacks with packing constraints that reflect the ~0.45 nm spacing found in XRD data.[29] Geometry optimizations were performed under periodic boundary conditions to assess the relative stabilities of these packing arrangements.

As shown in Fig. 7, MC dimers exhibit a significant energetic stabilization, approximately 3 kcal mol^{-1} lower in energy than their SP counterparts. This difference underscores the role of MC's planar, zwitterionic structure in promoting favorable π–π stacking and dipole–dipole interactions, which likely drive the formation of highly ordered nanosheets and nanotubes. In contrast, SP dimers are hindered by non-planarity and steric bulk, resulting in less favorable packing and reduced crystallinity.

To test whether this energetic preference persists in extended assemblies, molecular dynamics simulations were performed on fully solvated membrane models constructed from the two lowest-energy DFT-predicted SP and MC 1D packing motifs (see SI, Fig. S20). Using a customized peptoid force field, the MC membranes show a 10–15 kcal mol^{-1} per monomer stronger solute–solvent stabilization than their SP counterparts, consistent with the enhanced stability and crystallinity observed experimentally.

Together, the DFT and MD analyses provide a coherent mechanistic explanation for the experimental observations: SP-to-MC isomerization enhances the thermodynamic favorability of ordered assembly, directly linking molecular conformation to macroscopic morphology (see SI for details).

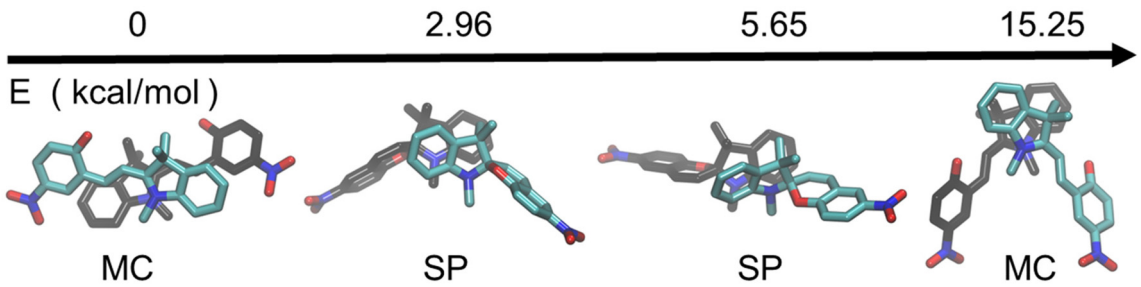

Fig. 7 DFT-optimized structures and relative energies of SP/SP and MC/MC dimers under periodic boundary conditions. The MC dimer is about 3.0 kcal mol^{-1} more stable than the SP dimer, reflecting more favorable stacking interactions due to its planar geometry and strong dipole alignment. Each dimer contains two monomers shown with distinct carbon colors (black and cyan) to highlight their relative orientations; nitrogen and oxygen atoms are shown in blue and red, respectively, and hydrogen atoms are omitted for clarity. This energetic preference explains the enhanced crystallinity and faster assembly observed experimentally for MC-functionalized peptoids compared to their SP analogues.

Stimuli-responsive peptoid crystalline nanomaterials as carbonic anhydrase (CA) mimics

Our recent study showed that peptoid crystalline nanomaterials containing Nhis groups can be used as CA mimics for enhanced hydration and sequestration of CO_2.[35] Because the hydrophilic domains of Pep1 and Pep2 both contain Nhis groups, we hypothesize that the assembled, stimuli-responsive nanomaterials from Pep1MC can be used as CA mimics exhibiting responsive catalytic properties. The high catalytic efficiency and specificity found in natural enzymes are from their ability to fold into well-ordered active site conformations through self-assembly.[34,49,50] We speculate that the assembly of highly crystalline Pep1MC nanosheets and Pep2MC nanotubes, respectively, which have a high density of ordered functional imidazole groups, will exhibit much higher efficiency as CA mimics compared to those assembled from Pep1SP or Pep2SP, which exhibit significantly lower crystallinity. To evaluate this, we employed a colorimetric assay that involved the hydrolysis of 4-nitrophenyl acetate (4-NPA) to 4-nitrophenol (4-NP) at room temperature. This reaction has been commonly used to evaluate the efficiency of CA mimics.[35] By monitoring the UV-Vis absorbance of 4-NP at 400 nm, the hydrolysis rate of the peptoid assemblies was determined. As shown in Fig. 8A, both Pep1MC and Pep2MC crystalline assemblies demonstrated significantly higher activity in the hydrolysis of 4-NPA compared to their SP-containing counterparts. These notable differences in hydrolysis efficiency can be attributed to the high crystallinity of the MC-containing peptoid assemblies, which contain highly ordered imidazole groups, thereby enhancing ester hydrolysis activity. This is consistent with the improved packing stability of MC dimers predicted by DFT. These findings align with our recent reports, in which peptoid-based highly crystalline nanosheets and nanotubes demonstrated significantly higher activity as biomimetic catalysts compared to their amorphous counterparts.[26,34,35,46] No significant difference was observed for the effect of assembly morphology on the catalytic activity, as both assembled Pep1MC and Pep2MC nanomaterials exhibited similar hydrolysis activities. To further illustrate the significance of crystallinity and the organized arrangement of active groups for catalytic activity, Pep1MC was exposed to ambient visible light for varying durations. This exposure resulted in a reduction in crystallinity and the disassembly of the tightly packed nanostructure as observed in Fig. 5. Subsequent hydrolysis tests with these altered samples revealed a decrease in their hydrolysis activity, which is likely due to the disruption of the crystalline assemblies (Fig. 8B). Pseudo rate constants derived from the hydrolysis rate also reveal superior activity from the MC-containing peptoid assemblies compared to the SP-containing assemblies (Table S1). Interestingly, both assembled Pep1MC and Pep2MC samples collected after the completion of the catalytic hydrolysis reactions retained their assembly morphology (Fig. S19), highlighting the excellent stability of these peptoid nanostructures. We expect that this stimuli-responsive crystalline peptoid assembly system could be used as a platform for the development of efficient CA mimics for enhanced hydration and sequestration of CO_2 [35] and for the development of other enzyme mimics.

Conclusions

In conclusion, we report the use of the conversion of spiropyran (SP) into merocyanine (MC) for the development of multi-stimuli responsive nanomaterials. We found that heat-mediated SP to MC transformation is highly efficient, and this property can be utilized for the tunable assembly properties of SP and MC functionalized peptoids. When peptoids were self-assembled in MC form, highly crystalline nanomaterials were obtained, whereas with SP form, amorphous-like materials

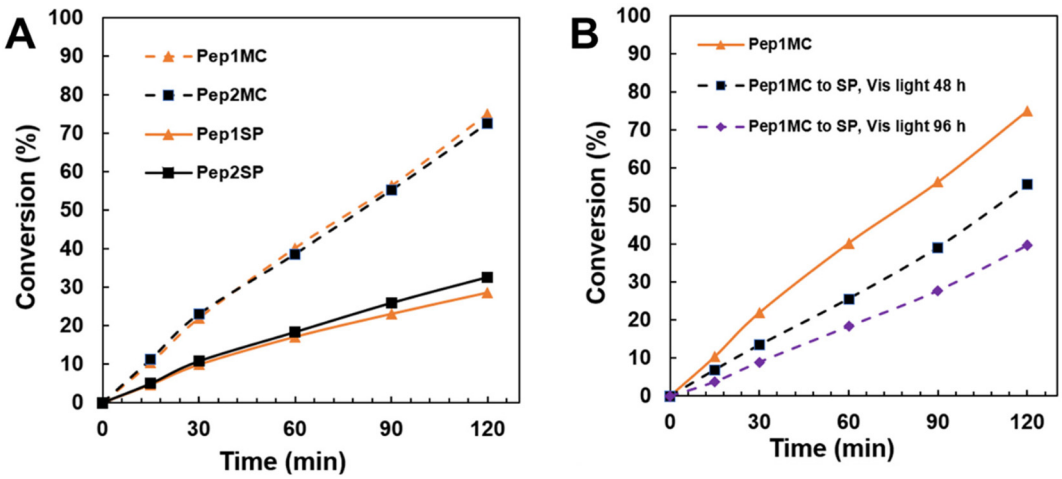

Fig. 8 (A) Comparison of 4-NPA conversion rate by various assembled peptoid catalysts with different crystallinity and morphology. (B) Comparison of the 4-NPA hydrolysis rate by assembled Pep1MC and Pep1MC samples with exposure to ambient light. Hydrolysis of 4-NPA was studied at [HEPES buffer] = 50 mM, [catalyst] = 0.125 mM, [4-NPA] = 0.25 mM at pH 7.4 and room temperature.

were observed. MC peptoid nanomaterials showed excellent stability in the absence of light; only upon exposure to visible light, disassembly of the crystalline nanostructures was observed due to the transformation into SP moieties. Periodic DFT calculations on SP and MC dimers further support these findings by revealing significantly more favorable packing energetics for MC, consistent with its enhanced crystallinity and assembly behavior observed experimentally. Finally, we demonstrated that the catalytic activity in ester hydrolysis can be tuned by the stimuli-responsive, reversible control of the crystallinity of SP- and MC-functionalized assembled nanomaterials. We envision that the functionalization of SP moieties into peptoids for stimuli-responsive assembly and disassembly properties will inspire a wide range of applications, including biomedical technology and biomimetic crystallization.

Methods

Materials

All materials were sourced from commercial suppliers and were used as received unless otherwise indicated.

Peptoid synthesis and self-assembly

The synthesis of all peptoid sequences was performed on rink amide resins, utilizing either manual or automated solid-phase synthesis methods detailed in our earlier publications, unless otherwise specified.[26,27] The specific synthesis protocols for each peptoid can be found in the SI. To cleave the synthesized peptoids from the resins, they were treated with 95% (v/v) trifluoroacetic acid (TFA) in water in a cartridge for one hour with agitation. The solution was then collected by filtration, and TFA was removed by evaporation under reduced pressure. After TFA evaporation, the crude samples were completely dissolved in an acetonitrile/water mixture and purified using reverse-phase high-performance liquid chromatography (HPLC) set up with an XBridgeTM Prep C18 OBDTM column, 10 μm, 19 mm × 100 with a linear gradient of 60–80% acetonitrile in water with 0.1% TFA. The collected fractions were analyzed with a UPLC (Waters, ACQUITY reverse-phase at 0.4 ml min^{-1} over 7 min at 40 °C with an ACQUITYBEH C18, 17 μm, and 2.1 mm × 50 mm column) connected with the MS system (Waters SQD2). The collected pure fractions were lyophilized to yield a slightly yellowish powder.

For peptoid self-assembly, one μmol of the corresponding lyophilized peptoid was dissolved in 200 μL of a 1 : 1 acetonitrile/water mixture, resulting in a slightly yellowish, clear solution of 5.0 mM concentration. The resulting SP-peptoid was allowed to sit at 4 °C for slow evaporation in the presence of ambient light, facilitating self-assembly. In the case of MC-peptoids, SP-peptoids were transformed into MC-peptoids by heating them at 60 °C for 20 minutes in the absence of light, resulting in a deep red solution. MC-peptoids were also self-assembled by initially exposing them to 365 nm UV light for one hour or by leaving them in a dark environment without heating. The resulting MC-peptoid solution was left at 4 °C in the absence of light to promote the slow evaporation of acetonitrile and facilitate self-assembly.

Characterizations

Nuclear magnetic resonance (NMR). NMR characterizations were conducted with a Bruker 500 MHz spectrometer.

Ultra-violet visible (UV-vis) spectroscopy. All UV-Vis spectroscopy analyses were performed using a Tecan Safire 2 microplate reader.

Atomic force microscopy (AFM). AFM imaging in air was performed using a Bruker Nanoscope 8 instrument in ScanAsyst mode with silicon probes (HQ: NSC19 Al/BS, μmasch) at ambient conditions. The sample was prepared by mixing 1.0 μl of self-assembled gel-like materials with 300 μl of deionized (DI) water, from which was 40 μl then placed onto a freshly cleaved mica substrate. After 5 minutes of incubation, excess water was removed from the mica surface by blotting with Whatman filter paper. Image processing and analysis were conducted using NanoScope Analysis software.

In situ AFM imaging was performed using silicon probes (SNL-C, spring constant: 0.24 N m^{-1}, tip radius: 2 nm; Bruker) in tapping mode on a Cypher ES AFM (Asylum Research). Peptoid assembly solutions were diluted with deionized water, and 80 μL of the diluted solution was deposited onto a freshly cleaved mica surface at room temperature. Image processing and analysis were conducted using Gwyddion SPM data analysis software.

Scanning electron microscopy (SEM). SEM imaging was performed using an Apreo Low Vac 2S microscope. The sample preparation mirrored that of the AFM, where 1.0 μl of self-assembled gel-like materials was added to 300 μl of DI water and then placed onto a silicon wafer. After a few minutes of incubation, the water was blotted away with Whatman filter paper, and the surface was dried using nitrogen gas.

Transmission electron microscopy (TEM). Aqueous solutions were directly drop-cast onto formvar/carbon-coated TEM grids (Ted Pella, 300 mesh) for transmission electron microscopy (TEM) and scanning transmission electron microscopy (STEM) sample preparation. The solutions remained on the grids for 10 minutes before being wicked away using filter paper. TEM and STEM imaging were conducted on a FEI Titan 80–300 Environmental TEM operated at 300 kV and equipped with an objective lens corrector. For HAADF-STEM imaging, the inner and outer collection angles of the annular dark-field detector were set to 55 and 220 mrad, respectively. Image acquisition and processing were carried out using Gatan Digital Micrograph.

X-ray diffraction (XRD) analysis. Powder XRD data were collected using a multiple-wavelength anomalous diffraction and monochromatic macromolecular crystallography beamline, 8.3.1 at the Advanced Light Source (ALS) located at Lawrence Berkeley National Laboratory. Data characterization and processing were performed according to the protocols reported in our previous studies.[27]

Computational methods

Global optimization of dimer structures. Monomer structures of SP and MC were generated from SMILES[51] strings and geometry-optimized using the GFN2-xTB method.[52] To identify representative packing motifs, dimer configurations of SP/SP and MC/MC were globally optimized using the ABCluster package,[53] which implements the artificial bee colony algorithm. A total of 1000 dimer structures were sampled per isomer and filtered based on geometric alignment and inter-amine (N–N) distances relevant to experimental backbone packing (~0.45 nm). The two lowest-energy dimers for each isomer were selected for further analysis.

Periodic dimer packing energetics. Periodic one-dimensional (1D) dimer stacks were constructed by aligning the N–N vector of each dimer along the *x*-axis and replicating under periodic boundary conditions in a 0.9 × 3.0 × 3.0 nm^3 simulation cell. Geometry optimizations were performed using the Quick Step module in CP2K package[54] with the revPBE functional,[55] Grimme D2 dispersion correction,[56] and a multigrid cutoff of 400 Ry. Each system was optimized under constant volume using analytical stress tensors. All calculations employed DZVP-MOLOPT basis sets[57] and matching GTH pseudopotentials.[58]

Relative total energies were used to compare the stability of MC and SP packing motifs under equivalent conditions. Energetic trends were verified by scanning the inter-dimer spacing along the *x*-axis to confirm a local minimum at approximately 0.45 nm.

Force-field molecular dynamics simulations. To extend the DFT-derived packing analysis to larger, solvated assemblies, molecular dynamics (MD) simulations were performed on fully constructed membrane models based on the two lowest-energy SP and MC 1D packing motifs, following the membrane construction protocol described in our previous work.[35] The simulations employed a customized peptoid force field developed using our STEPs framework[59,60] for systematic parameter optimization and validation against *ab initio* data. Systems were solvated with explicit TIP3P water, and energetic and structural analyses were conducted to evaluate solute–solvent stabilization and packing persistence. Complete parameterization procedures and simulation details are provided in the SI.

Author contributions

C. L. C. directed the project. P. C. conducted all the experimental study and characterization except as mentioned otherwise. B. S. H. and M. D. B. conducted the atomistic modelling. C. L. C. conducted XRD data collection of the peptoid assemblies. P. C. and C-L. C. analyzed the XRD data. C. S. assisted with *in situ* AFM characterization. B. H. conducted the TEM characterizations. K. W. assisted with NMR collection and analysis. P. C., B. S. H., M. D. B., and C. L. C. wrote the manuscript. All authors discussed the results and commented on the manuscript.

Conflicts of interest

There are no conflicts to declare.

Data availability

The data supporting the findings of this study are available within the article and its supplementary information (SI). All data are also available upon reasonable request from the corresponding author. Supplementary information is available. See DOI: https://doi.org/10.1039/d5nr03491d.

Acknowledgements

The development of peptoid nanosheets and DFT calculations were supported by the Department of Energy (DOE), Office of Basic Energy Sciences (BES), Division of Materials Science and Engineering, Biomolecular Materials Program under award FWP-65357 at Pacific Northwest National Laboratory (PNNL). The development of responsive peptoid materials was supported by DOE-BES as part of the Energy Frontier Research Centers program: CSSAS – The Center for the Science of Synthesis Across Scales – under Award Number DE-SC0019288 [FWP 72448 at PNNL]. The carbonic anhydrase mimic study was supported by the DOE-BES, Division of Materials Science and Engineering, Biomolecular Materials Program under an award FWP 80124 at PNNL. The force field development and simulation were supported by the DOE-BES, Division of Materials Science and Engineering, Biomolecular Materials Program, under an award FWP 77876 at PNNL. Work at the Molecular Foundry and X-ray diffraction at the Advanced Light Source (ALS) at Lawrence Berkeley National Laboratory (LBNL) was supported by the Office of Science, Office of Basic Energy Sciences, of the U.S. DOE under Contract DE-AC02-05CH11231. This research used resources of the National Energy Research Scientific Computing Center (NERSC), a DOE Office of Science User Facility located at LBNL, operated under Contract No. DE-AC02-05CH11231 using NERSC award BES-ERCAP0024465. PNNL is a multi-program national laboratory operated for the Department of Energy by Battelle under Contract No. DE-AC05-76RL01830. P. C. acknowledges Kennesaw State Academic Affairs for support of the NMR facility.

References

1 L. Shao, J. Ma, J. L. Prelesnik, Y. Zhou, M. Nguyen, M. Zhao, S. A. Jenekhe, S. V. Kalinin, A. L. Ferguson, J. Pfaendtner, C. J. Mundy, J. J. De Yoreo, F. Baneyx and C.-L. Chen, *Chem. Rev.*, 2022, **122**, 17397–17478.
2 Z. Li, B. Cai, W. Yang and C.-L. Chen, *Chem. Rev.*, 2021, **121**, 14031–14087.
3 J. Zhu, N. Avakyan, A. Kakkis, A. M. Hoffnagle, K. Han, Y. Li, Z. Zhang, T. S. Choi, Y. Na, C.-J. Yu and F. A. Tezcan, *Chem. Rev.*, 2021, **121**, 13701–13796.

4 S. Fleming and R. V. Ulijn, *Chem. Soc. Rev.*, 2014, **43**, 8150–8177.
5 A. Levin, T. A. Hakala, L. Schnaider, G. J. L. Bernardes, E. Gazit and T. P. J. Knowles, *Nat. Rev. Chem.*, 2020, **4**, 615–634.
6 L. Shao, D. Hu, S.-L. Zheng, T. K. H. Trinh, W. Zhou, H. Wang, Y. Zong, C. Li and C.-L. Chen, *Angew. Chem., Int. Ed.*, 2024, **63**, e202403263.
7 L.-J. Chen and H.-B. Yang, *Acc. Chem. Res.*, 2018, **51**, 2699–2710.
8 R. J. Mart, R. D. Osborne, M. M. Stevens and R. V. Ulijn, *Soft Matter*, 2006, **2**, 822–835.
9 S. Panja and D. J. Adams, *Chem. Soc. Rev.*, 2021, **50**, 5165–5200.
10 M. P. Hendricks, K. Sato, L. C. Palmer and S. I. Stupp, *Acc. Chem. Res.*, 2017, **50**, 2440–2448.
11 J.-F. Gohy and Y. Zhao, *Chem. Soc. Rev.*, 2013, **42**, 7117–7129.
12 K. Sun, Q.-Y. Lv, X.-L. Chen, L.-B. Qu and B. Yu, *Green Chem.*, 2021, **23**, 232–248.
13 K. Tashiro, M. Otori and S. Satokawa, *Chem. Commun.*, 2023, **59**, 4304–4307.
14 R. Klajn, *Chem. Soc. Rev.*, 2014, **43**, 148–184.
15 L. Kortekaas and W. R. Browne, *Chem. Soc. Rev.*, 2019, **48**, 3406–3424.
16 H. Görner and A. K. Chibisov, *J. Chem. Soc., Faraday Trans.*, 1998, **94**, 2557–2564.
17 A. M. Alfaraidi, B. Kudisch, N. Ni, J. Thomas, T. Y. George, K. Rajabimoghadam, H. J. Jiang, D. G. Nocera, M. J. Aziz and R. Y. Liu, *J. Am. Chem. Soc.*, 2023, **145**, 26720–26727.
18 A. de Vries, K. Goloviznina, M. Reiter, M. Salanne and M. R. Lukatskaya, *Chem. Mater.*, 2024, **36**, 1308–1317.
19 J. Sheng, J. Perego, S. Bracco, W. Czepa, W. Danowski, S. Krause, P. Sozzani, A. Ciesielski, A. Comotti and B. L. Feringa, *Adv. Mater.*, 2024, **36**, 2305783.
20 G. Das, T. Prakasam, N. Alkhatib, R. G. AbdulHalim, F. Chandra, S. K. Sharma, B. Garai, S. Varghese, M. A. Addicoat, F. Ravaux, R. Pasricha, R. Jagannathan, N. i. Saleh, S. Kirmizialtin, M. A. Olson and A. Trabolsi, *Nat. Commun.*, 2023, **14**, 3765.
21 H. Inaba, M. Sakaguchi, S. Watari, S. Ogawa, A. M. R. Kabir, A. Kakugo, K. Sada and K. Matsuura, *ChemBioChem*, 2023, **24**, e202200782.
22 W. Wang, J. Hu, M. Zheng, L. Zheng, H. Wang and Y. Zhang, *Org. Biomol. Chem.*, 2015, **13**, 11492–11498.
23 J. Sun and R. N. Zuckermann, *ACS Nano*, 2013, **7**, 4715–4732.
24 N. Gangloff, J. Ulbricht, T. Lorson, H. Schlaad and R. Luxenhofer, *Chem. Rev.*, 2016, **116**, 1753–1802.
25 B. Cai, Z. Li and C.-L. Chen, *Acc. Chem. Res.*, 2021, **54**, 81–91.
26 T. Jian, Y. Zhou, P. Wang, W. Yang, P. Mu, X. Zhang, X. Zhang and C.-L. Chen, *Nat. Commun.*, 2022, **13**, 3025.
27 H. Jin, Y.-H. Ding, M. Wang, Y. Song, Z. Liao, C. J. Newcomb, X. Wu, X.-Q. Tang, Z. Li, Y. Lin, F. Yan, T. Jian, P. Mu and C.-L. Chen, *Nat. Commun.*, 2018, **9**, 270.
28 Y. Li, G. Yang, L. Gerstweiler, S. H. Thang and C.-X. Zhao, *Adv. Funct. Mater.*, 2023, **33**, 2210387.
29 J. A. Hammons, M. D. Baer, T. Jian, J. R. I. Lee, T. M. Weiss, J. J. De Yoreo, A. Noy, C.-L. Chen and A. Van Buuren, *J. Phys. Chem. Lett.*, 2021, **12**, 6126–6133.
30 Y. Luo, Y. Song, M. Wang, T. Jian, S. Ding, P. Mu, Z. Liao, Q. Shi, X. Cai, H. Jin, D. Du, W.-J. Dong, C.-L. Chen and Y. Lin, *Small*, 2019, **15**, 1902485.
31 F. Jiao, X. Wu, T. Jian, S. Zhang, H. Jin, P. He, C.-L. Chen and J. J. De Yoreo, *Angew. Chem., Int. Ed.*, 2019, **58**, 12223–12230.
32 H. Jin, F. Jiao, M. D. Daily, Y. Chen, F. Yan, Y.-H. Ding, X. Zhang, E. J. Robertson, M. D. Baer and C.-L. Chen, *Nat. Commun.*, 2016, **7**, 12252.
33 F. Jiao, Y. Chen, H. Jin, P. He, C.-L. Chen and J. J. De Yoreo, *Adv. Funct. Mater.*, 2016, 8960–8967, DOI: 10.1002/adfm.201602365.
34 T. K. H. Trinh, B. Jin, R. N. Zuckermann and C.-L. Chen, *ACS Appl. Mater. Interfaces*, 2025, **17**, 44347–44359.
35 P. Chakma, Y. Chen, B. S. Harris, Y. W. Elhady, R. Zheng, M. E. Bowden, V. Shutthanandan, A. B. Bard, T. K. H. Trinh, X. Zheng, C. J. Mundy, M. D. Baer and C.-L. Chen, *Nat. Commun.*, 2025, **16**, 7348.
36 J. Ma, B. Cai, S. Zhang, T. Jian, J. J. De Yoreo, C.-L. Chen and F. Baneyx, *Nano Lett.*, 2021, **21**, 1636–1642.
37 H. Du, H. Trinh, O. C. Brandon, R. Zheng, H. Wang, K. Corry, T. R. Wood, C.-L. Chen and E. Nance, bioRxiv, 2025, 2025.2003.2006.641448. DOI: 10.1101/2025.03.06.641448.
38 Y. Song, X. Cai, M. Wang, D. Du, Y. Lin and C.-L. Chen, *Nano Res.*, 2024, **17**, 788–796.
39 J. Ma, B. Jin, K. N. Guye, M. E. Chowdhury, N. Y. Naser, C.-L. Chen, J. J. De Yoreo and F. Baneyx, *Adv. Mater.*, 2023, **35**, 2207543.
40 C. L. Chen and A. M. Beatty, *J. Am. Chem. Soc.*, 2008, **130**, 17222–17223.
41 C. L. Chen, H. Y. Tan, J. H. Yao, Y. Q. Wan and C. Y. Su, *Inorg. Chem.*, 2005, **44**, 8510–8520.
42 C. L. Chen, A. M. Goforth, M. D. Smith, C. Y. Su and H. C. zur Loye, *Angew. Chem., Int. Ed.*, 2005, **44**, 6673–6677.
43 C. L. Chen, C. Y. Su, Y. P. Cai, H. X. Zhang, A. W. Xu, B. S. Kang and H. C. zur Loye, *Inorg. Chem.*, 2003, **42**, 3738–3750.
44 C. L. Chen, C. Y. Su, Y. P. Cai, H. X. Zhang, A. W. Xu and B. S. Kang, *New J. Chem.*, 2003, **27**, 790–792.
45 C. L. Chen, J. Y. Zhang and C. Y. Su, *Eur. J. Inorg. Chem.*, 2007, 2997–3010, DOI: 10.1002/ejic.200700187.
46 T. K. H. Trinh, T. Jian, B. Jin, D.-T. Nguyen, R. N. Zuckermann and C.-L. Chen, *ACS Appl. Mater. Interfaces*, 2023, **15**, 51191–51203.
47 J. Zhou, Y. Li, Y. Tang, F. Zhao, X. Song and E. Li, *J. Photochem. Photobiol., A*, 1995, **90**, 117–123.
48 Y. Song, M. Wang, S. Akkineni, W. Yang, J. J. Hettige, H. Jin, Z. Liao, P. Mu, F. Yan, M. Baer, J. J. De Yoreo, D. Du, Y. Lin and C.-L. Chen, *ACS Mater. Lett.*, 2021, **3**, 420–427.
49 M. Raynal, P. Ballester, A. Vidal-Ferran and P. W. N. M. van Leeuwen, *Chem. Soc. Rev.*, 2014, **43**, 1734–1787.

50 A. R. Hirst, S. Roy, M. Arora, A. K. Das, N. Hodson, P. Murray, S. Marshall, N. Javid, J. Sefcik, J. Boekhoven, J. H. van Esch, S. Santabarbara, N. T. Hunt and R. V. Ulijn, *Nat. Chem.*, 2010, **2**, 1089–1094.
51 D. Weininger, *J. Chem. Inf. Comput. Sci.*, 1988, **28**, 31–36.
52 C. Bannwarth, S. Ehlert and S. Grimme, *J. Chem. Theory Comput.*, 2019, **15**, 1652–1671.
53 J. Zhang and M. Dolg, *Phys. Chem. Chem. Phys.*, 2015, **17**, 24173–24181.
54 J. Hutter, M. Iannuzzi, F. Schiffmann and J. VandeVondele, *Wiley Interdiscip. Rev.: Comput. Mol. Sci.*, 2014, **4**, 15–25.
55 Y. Zhang and W. Yang, *Phys. Rev. Lett.*, 1998, **80**, 890–890.
56 S. Grimme, *J. Comput. Chem.*, 2006, **27**, 1787–1799.
57 J. VandeVondele and J. Hutter, *J. Chem. Phys.*, 2007, **127**, 114105.
58 S. Goedecker, M. Teter and J. Hutter, *Phys. Rev. B: Condens. Matter Mater. Phys.*, 1996, **54**, 1703–1710.
59 B. S. Harris, K. K. Bejagam and M. D. Baer, *J. Phys. Chem. B*, 2023, **127**, 6573–6584.
60 Y. W. Elhady, B. S. Harris, C. J. Mundy and M. D. Baer, *J. Phys. Chem. B*, 2025, **129**, 5901–5912.